

# Polarimetric Features of GNSS-R Signal Over Land: A Simulation Study

Laura Dente<sup>1</sup>, Leila Guerriero<sup>1</sup>, *Member, IEEE*, Emanuele Santi<sup>2</sup>, *Senior Member, IEEE*, Mehrez Zribi<sup>3</sup>, *Senior Member, IEEE*, Davide Comite<sup>4</sup>, *Senior Member, IEEE*, and Nazzareno Pierdicca<sup>4</sup>, *Senior Member, IEEE*

**Abstract**—In view of the launch of the ESA HydroGNSS mission, whose receiver will measure both left and right-polarized global navigation satellite system reflectometry (GNSS-R) signal, this study analyses the features of dual-polarized signals by using simulations provided by the soil and vegetation reflection simulator (SAVERS) over both bare soil and forest. The reliability of GNSS-R dual-polarized simulations of SAVERS over land is first assessed by comparison with data collected in the frame of the GLOBAL navigation satellite system reflectometry instrument (GLORI) airborne campaigns. Then, the simulator is used to carry out a sensitivity analysis of left–right (LR) and right–right (RR) circularly polarized spaceborne GNSS-R signals to soil moisture (SM), soil roughness (SR), and forest biomass (BIO). The combinations of the two polarizations, such as ratio, difference, and normalized difference, are included in the analysis as well. The study evaluates also the SM effects on the horizontal-right (HR) and vertical-right (VR) polarized GNSS-R signal. The results show that the combination of the two circular polarizations can reduce the small-scale roughness effect in the SM monitoring as well as the effect of topography, and it can extend the sensitivity to large values of BIO. A critical point assessed by this study is the low value of the RR signal power, which may be difficult to detect over the noise floor, especially over land regions with low depolarization effects.

**Index Terms**—Biomass (BIO), Global Navigation Satellite System Reflectometry (GNSS-R), polarimetry, soil moisture (SM), soil roughness (SR).

## I. INTRODUCTION

THE global navigation satellite system reflectometry (GNSS-R) is a bistatic remote sensing technique exploit-

Manuscript received 22 December 2023; revised 30 April 2024; accepted 23 May 2024. Date of publication 5 June 2024; date of current version 20 June 2024. This work was supported in part by European Space Agency (ESA) in the frame of the HydroGNSS Scout Consolidation Study under Contract 4000129140/19/NL/CT. (*Corresponding author: Leila Guerriero.*)

Laura Dente was with the Department of Civil Engineering and Computer Science Engineering, Tor Vergata University of Rome, 00133 Rome, Italy. She resides in 7545RV Enschede, The Netherlands (e-mail: laura.dente@gmail.com).

Leila Guerriero is with the Department of Civil Engineering and Computer Science Engineering, Tor Vergata University of Rome, 00133 Rome, Italy (e-mail: leila.guerriero@uniroma2.it).

Emanuele Santi is with the Institute of Applied Physics, National Research Council, 50019 Florence, Italy (e-mail: e.santi@ifac.cnr.it).

Mehrez Zribi is with Centre d'Etudes Spatiales de la Biosphère (CNES/CNRS/INRAE/IRD/UPS), 31401 Toulouse, France (e-mail: mehrez.zribi@ird.fr).

Davide Comite and Nazzareno Pierdicca are with the Department of Information Engineering, Electronics and Telecommunications, Sapienza University of Rome, 00184 Rome, Italy (e-mail: davide.comite@uniroma1.it; nazzareno.pierdicca@uniroma1.it).

Digital Object Identifier 10.1109/TGRS.2024.3409880

ing the signal of GPS, GLONASS, Galileo, or other transmitters of GNSS constellations [1], [2]. A GNSS-R system is equipped with a receiver collecting the GNSS signal reflected by the Earth surface in specular and quasi-specular directions. The reflected signal is a source of information about the surface conditions due to its sensitivity to bio- and geophysical parameters. From the early 2000s, several experiments have demonstrated the sensitivity of GNSS-R observations to surface permittivity and vegetation parameters (see e.g., [3], [4], [5], [6], [7], [8]). More recently, the availability of U.K. TechDemoSat-1 (TDS-1) [9] and NASA Cyclone Global Navigation Satellite System (CyGNSS) data [10], as well as of soil moisture (SM) active and passive reflectometry (SMAP-R) data [11], has greatly stimulated the interest in the spaceborne GNSS-R technique for the monitoring of parameters related to land Essential Climate Variables [12], such as SM [13], forest biomass (BIO) [14], permafrost conditions [15], and wetland or inundation extension [16].

In this frame, an important contribution is expected to be given by HydroGNSS [17], the Scout Earth Observation small satellite mission approved by ESA and scheduled to be launched in 2025. The mission aims at using a constellation of two small satellites and novel GNSS reflectometry features to improve and enlarge the GNSS-R potentiality. The HydroGNSS receivers are designed to process both GPS and Galileo signals (both E1/L1 and E5/L5 frequencies), to provide both left- and right-hand circularly polarized data and to download complex data to characterize, when possible, the phase of the reflections with high sampling rate. These new features should lead to an improved coverage and resolution of the HydroGNSS data, with respect to the currently available GNSS-R data, and to disentangle the effects of SM, soil roughness (SR), and vegetation in the reflected signal, therefore improving the retrieval capability.

The main aim of this study is to support the HydroGNSS mission, identifying its added value for land monitoring. This study focuses on the evaluation of the potential contribution given by dual-polarized spaceborne GNSS-R data to the SM and the BIO retrieval. The analysis is mainly focused on the left–right (LR), and right–right (RR), (circularly transmitted and received) polarized signal, but the sensitivity of horizontal-right (HR), and vertical-right (VR), (circularly transmitted and linearly received) polarized signal to SM is analyzed as well. In the polarization acronyms, the convention used in this

manuscript associates the first letter with the receiver and the second with the transmitter.

At the time of this study, LR and RR GNSS-R data have been collected by ground-based and airborne sensors only [4], [5], [6], [18]. One experiment from a stratospheric balloon has been also reported in [8]. In 2015, the bandpass center frequency of the SMAP radar receiver was switched to GPS L2C band in order to enable GNSS-R measurements and to provide HR and VR polarized data [19]. With a refined calibration methodology, promising results have been achieved to assess the potential of SMAP-R data to monitor SM and freeze-thaw [20], [21]. Though LR and RR data could potentially be extracted from SMAP-R data, at the time of the writing of the present manuscript, those data were not yet publicly available and therefore they could not be used to validate simulations and results.

As spaceborne GNSS-R simultaneous LR and RR data are currently unavailable, the potential of this technique can only be investigated using a GNSS-R signal simulator. In this study, we rely on the soil and vegetation reflection simulator (SAVERS) [22]. SAVERS can simulate polarimetric GNSS-R observations taking into account the contribution of both soil and vegetation, specifically the forest electromagnetic properties and the topography. Originally developed for ground-based and airborne observations, SAVERS dual-polarized simulations were successfully validated against the measurements from the Land Monitoring with Navigation Signals (LEiMON) campaign [23] and from the GNSS Reflectometry Analysis for BIO monitoring (GRASS) campaign [6]. In the former experiment, a ground-based receiver was employed, whereas in the latter experiment, the receiver was installed on board an airplane. In both validation exercises, it was shown that SAVERS correctly simulates left-polarized signals, whereas it simulates a larger dynamic range of the right-polarized signal power than the observed one. Indeed, SAVERS estimated a much lower noise-free right-polarized power than the observed one, suggesting that the noise floor of the receiving instrument was reached. The ground-based experiment in [24] reports also the correct simulation of right-polarized attenuation and scattering of GNSS signals from a forest canopy.

The upgraded version of SAVERS for the case of spaceborne GNSS-R systems was presented in [25] and validated against TDS-1 data. The validation results show the capability of SAVERS to correctly simulate the topography effect and the vegetation attenuation of the left-polarized signal. SAVERS performance has been compared also with simulations carried out by other two GNSS-R simulators and against the delay Doppler map (DDM) collected by CYGNSS over the San Luis Valley validation site [26]. The three models, although based on different approaches, generally agree in the representation of the reflection and scattering properties of bare soils.

After describing the theoretical background of the polarimetric simulations in Section II of the present article, the accuracy of SAVERS dual-polarized simulations is further evaluated in Section III by comparing them with airborne data of the GLOBal navigation satellite system Reflectometry Instrument (GLORI) [27]. Then, in Section IV, SAVERS simulations for the case of a spaceborne system are used to carry out a sensitivity analysis of dual-polarized GNSS-R reflectivity

to SM, SR, and forest BIO. The conclusions summarize the potential of the combined use of left- and right-polarized data for the land monitoring.

## II. SAVERS SIMULATOR

A sensitivity analysis for the GNSS-R signal cannot be performed on the basis of the bistatic scattering coefficient alone because the resolution of GNSS-R measurements cannot be defined in a univocal way, see for example [1]. Indeed, the bistatic scattering coefficient can be extracted from monostatic radar measurements through inversion of the radar equation and normalization to the active area. For GNSS-R, instead, the active area depends not only on the incidence angle (IA) and on the platform altitude, but also on the scattering regime (coherent or incoherent), and the coherent and incoherent integration time. In other words, it is not possible to derive a GNSS-R scattering coefficient that depends on the surface parameters only, and the sensitivity analysis cannot be carried out overlooking the received power that can be modeled through the GNSS-R radar equation.

The SAVERS simulator and its updated version for spaceborne observations have been described and validated in several studies [12], [22], [23], [25], [26] and it is used in this work. The simulator computes the DDM of the reflected GNSS-R signal using the integral bistatic radar equation [28], weighting the bistatic scattering coefficient of all scatterers on the surface by the woodward ambiguity function (WAF). The bistatic scattering coefficient is made up of two components: the quasi-specular reflection of the surface [29], as well as the incoherent diffuse component due to the vegetation volume [2] and to the rough soil [30]. SAVERS simulates them both simultaneously, thus allowing a continuous and consistent transition from coherent to incoherent scattering regime. Indeed, as surface roughness and vegetation BIO increase, incoherent scattering becomes more and more important, and the model applicability for the frequency and the roughness scales used here have been proven in the literature [24], [29], [30].

Thanks to the simulation of the bistatic radar equation, SAVERS takes into account antenna and receiver parameters, which also determine the size of the active scattering area [29]. For example, in the GLORI airborne campaign, the GNSS-R signal comes from the whole antenna footprint, while in the TDS-1 spaceborne configuration, the signal is chip-limited.

The bistatic radar equation allows for simulating the GNSS-R signal received at any polarization, provided the polarimetric bistatic scattering cross-section  $\sigma_{rt}$  is modeled. To this end, the polarimetric covariance matrix  $\underline{\mathbf{C}}$  has been introduced into the electromagnetic modules of SAVERS. For a natural random target, it turns out that [31]

$$\sigma_{rt} = 4\pi \mathbf{B} \cdot \underline{\mathbf{C}} \mathbf{B}^*. \quad (1)$$

Given the polarization unit vector  $\mathbf{p}^r$  of the receiving antenna, and the polarization unit vector  $\mathbf{p}^t$  of the transmitting antenna, the vector  $\mathbf{B}$  is defined as follows:

$$\mathbf{B} = \begin{bmatrix} p_v^r p_v^t \\ p_v^r p_h^t \\ p_h^r p_v^t \\ p_h^r p_h^t \end{bmatrix} \quad (2)$$

where  $p_v$  and  $p_h$  are the vertical and horizontal components of  $\mathbf{p}'$  or  $\mathbf{p}^t$ .  $\mathbf{B}^*$  is the conjugate of  $\mathbf{B}$ . The covariance matrix is given by the following equation:

$$\underline{\mathbf{C}} = \begin{bmatrix} \langle S_{vv} S_{vv}^* \rangle & \langle S_{vv} S_{vh}^* \rangle & \langle S_{vv} S_{hv}^* \rangle & \langle S_{vv} S_{hh}^* \rangle \\ \langle S_{vh} S_{vv}^* \rangle & \langle S_{vh} S_{vh}^* \rangle & \langle S_{vh} S_{hv}^* \rangle & \langle S_{vh} S_{hh}^* \rangle \\ \langle S_{hv} S_{vv}^* \rangle & \langle S_{hv} S_{vh}^* \rangle & \langle S_{hv} S_{hv}^* \rangle & \langle S_{hv} S_{hh}^* \rangle \\ \langle S_{hh} S_{vv}^* \rangle & \langle S_{hh} S_{vh}^* \rangle & \langle S_{hh} S_{hv}^* \rangle & \langle S_{hh} S_{hh}^* \rangle \end{bmatrix} \quad (3)$$

where  $\underline{\mathbf{S}}$  is the target scattering matrix (whose elements are given by the appropriate electromagnetic approximation and are defined in the BSA convention) and  $\langle \cdot \rangle$  represents the ensemble average of different target realizations. In a GNSS-R system,  $\mathbf{p}^t$  is the polarization vector of a right circularly polarized wave. In this article, we present simulations carried out considering a receiving antenna with left and right circular polarizations or with horizontal and vertical linear polarizations since these are the polarization modes of the currently available GNSS-R spaceborne data. However, the approach adopted by SAVERS (i.e., with the inclusion of the bistatic scattering coefficient given by (1) in the bistatic radar equation) allows simulations of fully polarimetric data and compact polarimetric data [32].

When dealing with circular polarization, the polarization mismatch of the receiver and the transmitter is conventionally quantified selecting the relevant polarization vectors. In this study, we have simulated the antenna polarization mismatch assuming that the circularly polarized antennas are formed by a couple of electrical dipoles as described in [22].

All simulations are carried out without taking into account the noise, neither thermal nor speckle noise.

Once the signal received by the down-looking antenna is computed using the bistatic radar equation [28] (i.e.,  $Y_{rt}(\Theta, \tau, f)$  function of the time delay  $\tau$ , of the Doppler frequency  $f$  and of the target observation angle and dielectric properties included in the vector parameter  $\Theta$ ), SAVERS provides as output the normalized DDM (nDDM), that represents the power ratio of the signals received by the down-looking antenna and the signal received by the up-looking antenna, assuming the same coherent integration time

$$nDDM_{rt}(\Theta, \tau, f) = \frac{|Y_{rt}(\Theta, \tau, f)|^2}{|Y_{RR}^{UP}|^2}. \quad (4)$$

The signal at the up-looking antenna  $Y_{RR}^{UP}$  is defined as follows:

$$|Y_{RR}^{UP}|^2 = \frac{\lambda^2}{(4\pi)^2} P_T T_i^2 \frac{G_T(\vartheta_i) G_R^{UP}(\vartheta_i)}{R_{TR}^2}. \quad (5)$$

$R_{TR}$  is the distance between the transmitter and the receiver and  $G_R^{UP}$  is the up-looking antenna gain pattern.  $\lambda$ ,  $P_T$ , and  $G_T$  are the transmitted signal wavelength, the power, and the antenna gain of the transmitter, respectively.  $\vartheta_i$  is the IA and  $T_i$  is the coherent integration time.

The following analysis concerns the reflectivity observable computed from the peak of the simulated DDMs normalized to the incident power:

$$\Gamma_{rt}^{eq}(\Theta) = \max(nDDM_{rt}) \frac{G_R^{UP} (R_R + R_T)^2}{G_R R_{TR}^2} \quad (6)$$

where  $R_R$  is the distance from the receiver to the specular point (SP),  $R_T$  from the transmitter to the SP, and  $G_R$  is the down-looking antenna gain pattern. The detailed definition of this observable is reported in [25]. It is worth reminding that this observable is an equivalent reflectivity, since the signal is scattered from a finite surface, and it encompasses both coherent and incoherent components of the scattered field [12], [14], [25], [29]. In other words,  $\Gamma^{eq}$  is the reflectivity that would be observed if the measured power originated from coherent reflection only.

System and land surface parameters are all given as input data to SAVERS that also includes a digital elevation model (DEM) of the observed area to simulate topographic effects [25]. The DEM provides the local slope and aspect of the surface, which are taken into account in the quasi-specular and incoherent scattering modeling, as well as in the polarization rotation. Indeed, slope and elevation of surface facets within a resolution cell affects the delay and the intensity of the GNSS-R signal [25, Fig. 15]. The DEM can be included in airborne- or ground-based simulations, however, the topography effects are more significant in spaceborne measurements. This is due to the decreased resolution of the satellite GNSS-R measurements [1], so that the local IA shows more variability in spaceborne acquisitions with respect to airborne- or ground-based acquisitions because of topography. SAVERS simulations of left-hand circularly polarized signals were validated against TDS-1 observations over both bare soils with complex topography and open and dense forests [25], and against CyGNSS data over bare soils [26]. The validation studies showed a good agreement between the simulations and the observations over different sites, demonstrating the capability of SAVERS to correctly simulate the effect of the topography and the forest attenuation.

### III. COMPARISON OF POLARIMETRIC SIMULATIONS AND AIRBORNE DATA

The reliability of SAVERS circular dual-polarized simulations is experimentally assessed in this study using the data acquired in the GLORI campaign reported in [27]. The campaign was carried out in 2015 in the Southwest of France collecting airborne polarimetric GNSS-R data over the Landes forest (mainly constituted by maritime pines) and agricultural fields (cereals, corn, potato, and soybean). More details about this campaign can be found in [18] and [27].

Fig. 1 (top panel) shows the RR circularly polarized reflectivity versus the LR circularly polarized reflectivity observed by the GLORI instrument. The reflectivity observable was obtained following the approach described in [18]. The color bar refers to the IA (in degree) and the red line shows the linear regression function whose equation is reported inside the plot. Two filters were applied on the data for both polarizations: IA smaller than  $40^\circ$  (to neglect observations outside the antenna beamwidth) and LR reflectivity lower than  $-5$  dB (to avoid the observations over water bodies). RR reflectivity is generally lower than the LR reflectivity, with RR ranging between  $-35$  and  $-15$  dB, and LR being larger than  $-30$  dB. Both polarizations reach a saturation in the minimum value.

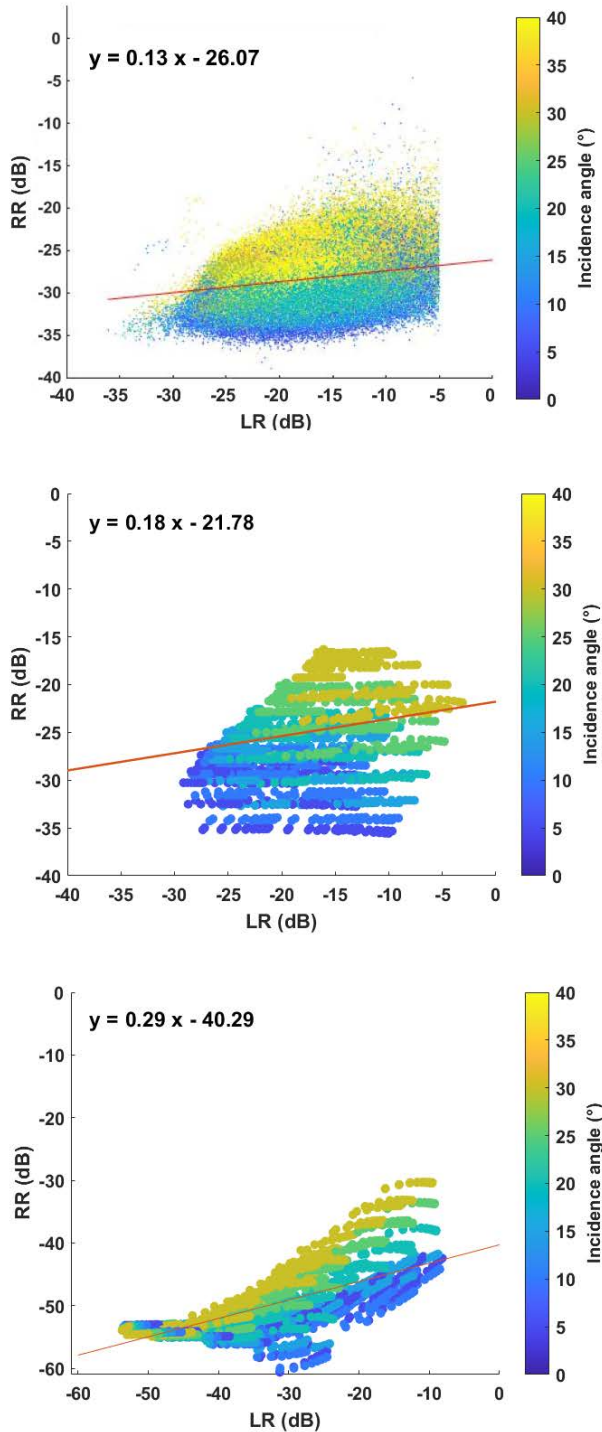


Fig. 1. GNSS-R reflectivity for RR polarization versus LR polarization (axes are in dB, colorbar reports the IA in degree). (Top) Data from GLORI campaign. (Middle) Simulated data for an airborne platform. (Bottom) Simulated data for a spaceborne platform.

RR reflectivity is clearly dependent on the IA, whereas this effect is much weaker on the LR, as it can also be observed from the analysis of the Fresnel reflection coefficients in the considered range of IA and from the experimental results reported in [12].

In order to investigate the capability of SAVERS to correctly simulate dual-polarized data, the simulator was run assuming

TABLE I  
SAVERS INPUTS FOR THE AIRBORNE SYSTEM AND FOR THE SPACEBORNE SYSTEM

	Airborne system	Spaceborne system
Operating frequency	GPS L1	GPS L1
Average altitude	600 m	825 km
Average speed	100 m/s	10.4 km/s
Coherent Integration time	1 ms	1 ms
Antenna pattern	Cosinusoidal	TDS-1 pattern
3dB antenna beamwidth	30°	30°

an airborne receiver with the same characteristics of the GLORI instrument (Table I reports the system parameters of the airborne receiver simulated by SAVERS) and assuming realistic surface conditions and input parameter ranges for the areas observed during the campaign. The following cases were simulated: dense softwood forest with a BIO ranging between 25 and 400 t/ha; open hardwood forest with BIO ranging between 5 and 40 t/ha; very small but dense trees with BIO ranging between 5 and 40 t/ha (this latter case was included to simulate the fields with short vegetation).

For all these cover classes, the IA was varied from 5° to 30°, the volumetric SM was varied from 5% to 40%, and the SR height standard deviation was varied from 0.5 to 3.0 cm. It was not possible to carry out a point-by-point validation since no detailed in situ data were available in the frame of this study, to be used as SAVERS inputs. Rather, a comparison is performed against the variability ranges of the simulations with those of the observation.

The scatter plot of RR versus LR reflectivity simulated by SAVERS is reported in the middle panel of Fig. 1. There is a general good agreement between the two top scatterplots of Fig. 1, with a similar distribution of the points in the reflectivity ranges. The slope and intercept of the linear fit of simulated data are slightly higher than the observed ones. This can be due to the differences between the assumed land cover features and the in situ one.

The bottom panel of Fig. 1 shows the scatter plot of the RR versus LR reflectivity simulated for the case of a spaceborne receiver (having the same characteristics of the TDS-1 receiver) and for the same surface and vegetation parameters used for the middle plot. Table I reports the system parameters that are used to simulate the spaceborne system (these were used for the sensitivity analysis as well).

Due to the higher receiver altitude and the path losses, the simulations for a spaceborne receiver reach much lower equivalent reflectivity values than those for an airborne receiver since, as mentioned in Section II, the equivalent reflectivity embeds both coherent and incoherent scattering. In particular, the observed surface is neither infinite nor plane, so that reflectivity does not exclusively represent a physical property of the surface, which by definition is independent of system parameters or range.

Even though it is not possible to carry out a point-by-point comparison, the plots of Fig. 1 show that SAVERS circular dual-polarized simulations have features similar to the

experimental data, such as similar variations with the IA, same dynamic ranges, and similar distribution of the points in the scatter plots. This leads to the conclusion that SAVERS is a suitable tool to investigate the potential of GNSS-R spaceborne polarimetric data.

#### IV. SENSITIVITY ANALYSIS

In this section, SAVERS simulations were used to carry out a sensitivity analysis of both LR and RR reflectivity to SM, SR, and forest BIO. We also consider the case of a linear receiving antenna, thus collecting HR and VR polarizations. The analysis was repeated both excluding and including the effect of the topography. The potential of a combined use of the two polarizations was investigated as well, by extending the sensitivity analysis to the polarization ratio (RR/LR and VR/HR), polarization difference (LR-RR and HR-VR), and normalized polarization difference [ $\text{NPD}_{L,R} = (\text{LR}-\text{RR})/(\text{LR} + \text{RR})$  and  $\text{NPD}_{H,V} = (\text{HR} - \text{VR})/(\text{HR} + \text{VR})$ ]. All of the above (i.e., ratio, difference, and NPD) were computed in linear units and then converted to dB to plot the results. As it will be better explained later, the computation in linear units allows for removing the disturbing factors in the sensitivity to SM and BIO, whereas this is not possible when the computation is done in dB.

For this analysis, a spaceborne GNSS-R receiver having the same system configurations of TDS-1 was assumed (see Table I). In particular, positions and velocity of receiver and transmitter were extracted from the GNSS-R data available at the Measurement of Earth Reflected Radio-navigation signals By Satellite (Merrbys) portal (<http://merrbys.co.uk>) under a Creative Commons Attribution, Non-Commercial 4.0 International License.

A bare soil was assumed to evaluate the sensitivity to SM and a boreal forest for the sensitivity study to BIO. The variability range of the IA was set from  $5^\circ$  to  $60^\circ$ . However, it must be underlined that only a small percentage of acquisitions by a GNSS-R system like TDS-1 or HydroGNSS owns an IA larger than  $50^\circ$ . To support this statement, the SPs in GNSS-R tracks were simulated assuming both a nadir looking antenna (as in TDS-1) and an antenna inclined by  $20^\circ$  (like CYGNSS and HydroGNSS). The SPs of the tracks were simulated for 1 month and, for each satellite position, the four highest received powers were selected. This selection was accomplished assuming a constant and polarization-independent reflectivity along all tracks. The SP distance from the receiver was taken into account, as well as the antenna pattern. The latter has been simulated as the typical pattern of GNSS-R receiver, i.e., an antenna with a  $-3$  dB beamwidth of about  $30^\circ$ , a  $-10$  dB beamwidth of about  $50^\circ$ , and first-null beamwidth of about  $80^\circ$ . This means that the power reflected by a SP observed with an IA larger than  $45^\circ$  is reduced by more than 10 dB, even if the antenna is inclined with respect to nadir. The simulations showed that, for a nadir-looking antenna, more than 95% of the SPs observed in 1 month has an IA lower than  $40^\circ$ . If the GNSS-R antenna is inclined at  $20^\circ$ , the SPs observed at an IA larger than  $45^\circ$  are only 15% of the total (which is more than 10 350 000).

TABLE II

MEAN VARIATIONS OF LR, RR, RR/LR, LR-RR, AND  $\text{NPD}_{L,R}$  FOR THE VARIATION OF SM FROM 5% TO 40%, OF SR FROM 0.5 TO 3 CM AND OF IA FROM  $5^\circ$  TO  $60^\circ$ . CASE STUDY: BARE SOIL

	LR	RR	RR/LR	LR-RR	$\text{NPD}_{L,R}$
$\Delta_{SM}$ (dB)	6.4	1.7	-4.8	7.5	1.4
$\Delta_{SR}$ (dB)	-11.9	-11.9	6e-4	-11.9	-5e-5
$\Delta_{IA}$ (dB)	5.9	50.2	44.3	2.1	-5.6

In the following, we report plots of the observable of interest as a function of the SM or the BIO for different roughness and IAs. Moreover, the sensitivity to the parameter  $i$ , where  $i$  is SM, SR, IA, or BIO, is quantified by computing the variation  $\Delta_i$  of the observable with the  $i$ th input (e.g., SM) increasing from its minimum to maximum value, and then averaging all the  $\Delta_i$  obtained varying the other inputs (e.g., SR and IA).

##### A. Sensitivity to Soil Moisture and Soil Roughness Without Topography

The sensitivity to SM and SR was first analyzed, considering a bare surface without large-scale topographic features (i.e., the elevation is set to a constant value). The IA ranged between  $5^\circ$  and  $60^\circ$  (with a step of  $5^\circ$ ), the volumetric SM varied from 5% to 40% (with a step of 5%), and the small scale SR was set to 0.5, 1.5, and 3 cm. A correlation length of 5 cm and an exponential autocorrelation function were used for all simulations. The mean variations of the observables are reported in Table II for the case of a topographically flat bare soil. Fig. 2 shows the simulated reflectivity as a function of the SM for the cases of: a single circular polarization, the ratio, the difference, and the  $\text{NPD}_{L,R}$ . To simplify the plots, only the simulations for smooth and rough soil surface and for  $10^\circ$ ,  $20^\circ$ ,  $40^\circ$ , and  $60^\circ$  IA are reported.

Fig. 2(a) and the first column of Table II show that the LR polarized signal is clearly sensitive to the SM (approximately 1.8 dB for a 10% variation of SM), but it is also very sensitive to the SR. Whereas, the sensitivity of LR to the IA increases with the roughness. The RR polarized reflectivity [Fig. 2(b)] can reach much lower values than LR, in particular at low IAs and for rough surfaces. RR is slightly sensitive to the SM and strongly to the IA (see Table II). The RR reflectivity shows a sensitivity to SR similar to LR; they both decrease by approximately 12 dB when the SR increases from 0.5 to 3.0 cm (about 4.8 dB for a variation of SR of 1 cm). The similar sensitivity of the two polarizations to SR suggests combining LR and RR in order to obtain a parameter independent of the roughness. As the surface roughness is a factor of the exponential function in the formulation of the bistatic scattering coefficient for both polarizations, the ratio (computed in linear units) of the two polarizations or the  $\text{NPD}_{L,R}$  removes the roughness factor. On the contrary, this is not the case for the polarization difference and when ratio and  $\text{NPD}_{L,R}$  are computed in dB.

The polarization ratio RR/LR shows a relatively good sensitivity to SM (approximately  $-1.4$  dB for 10% SM variation), without the disturbing effect of the SR [see Fig. 2(c)]. The continuous line (for a smooth surface) and the dashed-dotted line (for a rough surface) in Fig. 2(c) are overlapped and

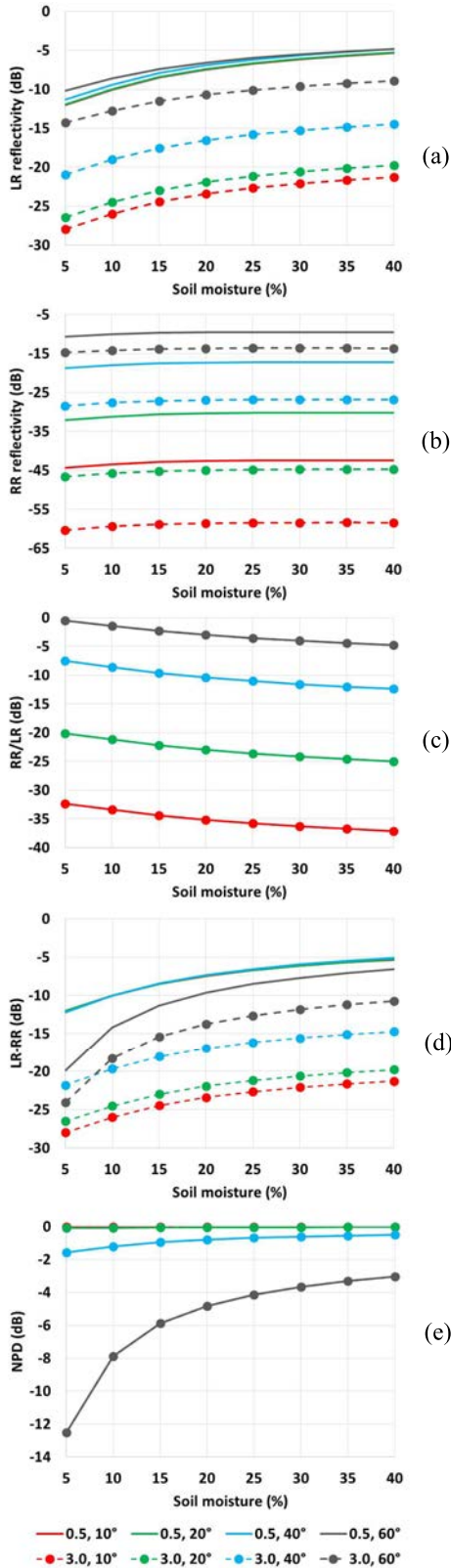


Fig. 2. GNSS-R circularly polarized reflectivity of bare soil versus the SM for SR 0.5 cm (continuous line) and 3.0 cm (dashed-dotted line) and for IA 10° (red), 20° (green), 40° (blue), and 60° (gray). (a) LR, (b) RR, (c) RR/LR, (d) LR-RR, and (e)  $NPD_{L,R}$ .

the variation of the ratio due to the roughness increase,  $\Delta_{SR}$ , is very small (Table II). The ratio is, however, strongly dependent on the IA, like RR.

TABLE III

MEAN VARIATIONS OF HR, VR, VR/HR, HR-VR, AND  $NPD_{H,V}$  FOR THE VARIATION OF SM FROM 5% TO 40%, OF SR FROM 0.5 TO 3 CM AND OF IA FROM 5° TO 60°. CASE STUDY: BARE SOIL

	HR	VR	VR/HR	HR-VR	$NPD_{H,V}$
$\Delta_{SM}(\text{dB})$	5.7	9.3	3.6	2.3	-4.0
$\Delta_{SR}(\text{dB})$	-11.9	-11.9	-1e-5	-11.9	4e-4
$\Delta_{IA}(\text{dB})$	8.6	-2.3	-10.9	28.2	22.0

The polarization difference is almost equal to the LR reflectivity for low IAs up to 40° [see Fig. 2(d)] as, for a bare and flat (no topography) surface, the RR signal is much lower than LR. As the IA increases, the RR reflectivity reaches values similar to the LR reflectivity and therefore the polarization difference (in dB) is much smaller than LR, for low SM values in particular.

The sensitivity of the  $NPD_{L,R}$  to the SM is almost negligible at low IAs, but a clear increase of this parameter with the SM can be observed at high IAs [Fig. 2(e)]. It is worth mentioning that it is not possible to compare the sensitivity index of the  $NPD_{L,R}$  to the one of the other observables because of the different dynamic ranges of the  $NPD_{L,R}$ . The latter is quite limited because of the low values of RR reflectivity.

The sensitivity analysis was repeated assuming a GNSS-R satellite system with the same characteristics of TDS-1, in terms of satellite height, antenna pattern, antenna gain, integration time, and DDM size and spacing, but with a linearly polarized receiving antenna. The simulation results are reported in the plots of Fig. 3, for HR and VR reflectivity, VR/HR polarization ratio, HR-VR polarization difference and  $NPD_{H,V} = (HR - VR)/(HR + VR)$  normalized polarization difference. Also for the linear polarizations, all parameters were calculated in linear units and then reported in dB in the plots. Table III reports the mean variations of the observables.

The HR and VR reflectivity of a flat bare soil are very close to each other [see Fig. 3(a) and (b)] when the IA is lower than 40°, and about 3 dB lower than the LR reflectivity, as expected and explained in detail in Appendix A. In fact, the incident right-polarized wave may be decomposed into a vertical and a horizontal polarized wave, each one carrying half of the right-polarized one. Each component is then reflected (or scattered) according to the corresponding linear Fresnel reflection coefficient (or bistatic scattering coefficient). For IAs very close to nadir, the two components are reflected (or scattered) in equal proportion, so that the HR and VR signals are 3 dB below the LR signal (see Appendix A). When the IA increases, the VR reflectivity is lower than HR. This was also observed with the data collected at about 40° IA over bare soils in the SMAP-R experiment reported in [19].

Both HR and VR are sensitive to the SM, increasing on average by 1.6 and 2.8 dB for every 10% increase of the SM, respectively, and they are strongly dependent on the SR (Table III). The sensitivity of HR and VR to the IA increases with the roughness.

The polarization ratio VR/HR has the advantage to be independent of the SR, but its sensitivity to the SM strongly depends on the IA [see Fig. 3(c)]. At low IAs this sensitivity

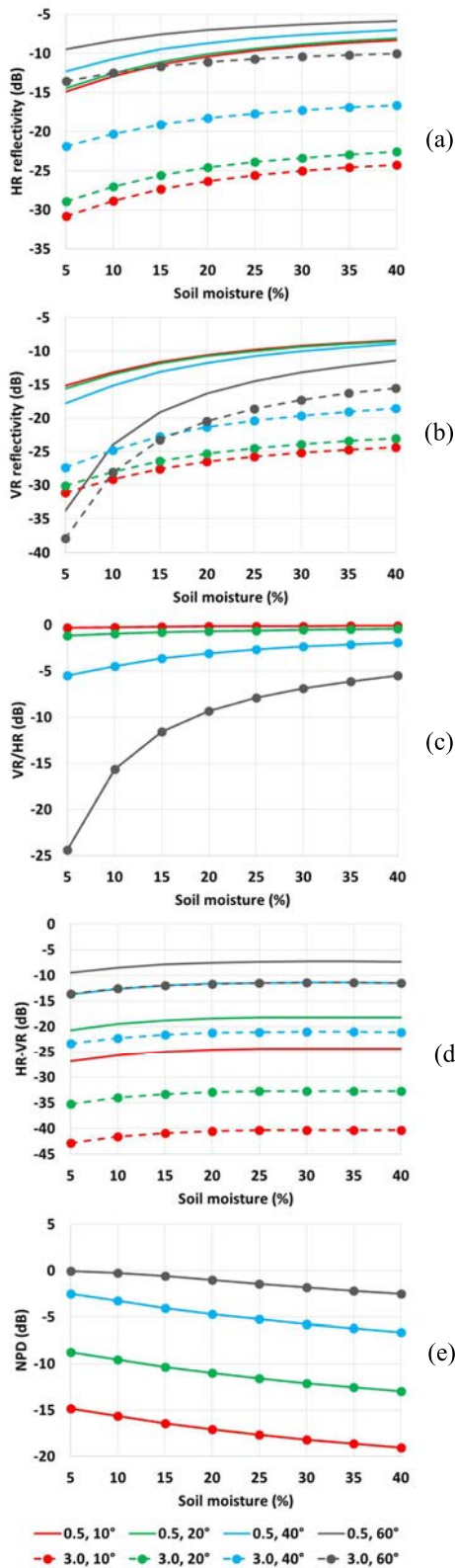


Fig. 3. GNSS-R linearly polarized reflectivity of bare soil versus the SM for SR 0.5 cm (continuous line) and 3.0 cm (dashed-dotted line) and for IA 10° (red), 20° (green), 40° (blue), and 60° (gray). (a) HR, (b) VR, (c) VR/HR, (d) HR-VR, and (e) NPD<sub>H,V</sub>.

is very weak, but at 60° IA the VR/HR ratio increases of about 20 dB when the SM increases from 5% to 40%.

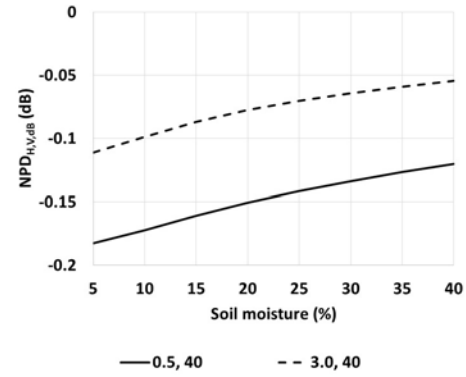


Fig. 4. Normalized polarization difference NPD<sub>H,V,dB</sub> of the linearly polarized reflectivity computed in dB at 40° IA and for smooth (0.5 cm) and rough (3.0 cm) bare soil.

The polarization difference HR-VR has a weak sensitivity to SM but a strong sensitivity to SR and IA [Fig. 3(d)]. Instead, NPD<sub>H,V</sub> is not sensitive to SR, but it is much sensitive to the IA. Assuming the IA effect can be predicted, its sensitivity to the SM keeps almost constant at different IAs up to 40° [see Fig. 3(e)].

LR, HR, VR, and LR-RR have the highest sensitivity to SM among all the observables but they depend on the SR as well. RR/LR and NPD<sub>H,V</sub> have a relatively lower sensitivity to SM, but these two observables have the important potentiality to single out the SM effect, as they do not depend on the small-scale roughness of the observed surface. Moreover, their sensitivity to SM does not change with the IA.

The reliability of the results obtained for the linearly polarized reflectivity can be evaluated against the results obtained with SMAP-R data. The GNSS-R system simulated by SAVERS in this study is different from the SMAP-R systems in terms of the receiving antenna pointing, gain, and pattern. Moreover, a different calibration method was used in this study to obtain the reflectivity. Therefore, it is not possible to directly compare HR- and VR-simulated reflectivity with those observed by SMAP-R. However, it is possible to compare the normalized polarization difference at 40° IA, as it is not affected by the differences between the simulated and the SMAP-R antenna and between the calibration methods. The NPD<sub>H,V</sub> obtained from SMAP-R data observed over the agricultural fields of the Corn Belt area in USA, when the fields were bare both in the sowing season and after harvesting, was reported in [33, Fig. 15].

However, in that case, the normalized polarization ratio was computed in dB (and not in linear units), i.e.,  $NPD_{H,V,dB} = (HR_{dB} - VR_{dB}) / (HR_{dB} + VR_{dB})$ . For comparison, NPD<sub>H,V,dB</sub> was computed in the present study as a function of the SM for a smooth and for a rough bare soil and at 40° IA, and the results are reported in Fig. 4.

Since detailed ground truth for soil and vegetation is not available for the corn belt data, a point-by-point model simulation is not possible. However, considering a generic SR variability from smooth to rough, the simulated NPD<sub>H,V,dB</sub> is in a good agreement with that reported in [33, Fig. 15(a)] in terms of variability range and sensitivity to SM. This confirms

the reliability of SAVERS simulations for the case of linearly polarized signal.

Fig. 4 shows that the normalized polarization difference is still dependent on the surface roughness when each term of the ratio is given in dB. Instead, in order to single out the sensitivity to the SM, it is preferable to compute the NPD from the reflectivity in linear units.

In general, HR and VR observables are very similar in a feasible range of IAs for GNSS-R systems, so that it can be difficult to exploit their information content in a retrieval algorithm. Additionally, being lower than LR, both linearly polarized signals can exhibit low signal-to-noise ratio (SNR), especially when mountainous and/or vegetated areas are observed, and therefore their detection requires high-gain antennas, as in the SMAP-R experiment.

It is worth stressing that the linearly polarized signals suffer from the Faraday rotation effect, and they call for a specific compensation during the calibration procedure, as it has been done for SMAP-R data [20]. On the contrary, the ionosphere produces only a phase change on the elliptical signal reflected from the Earth, without introducing any amplitude variation (see Appendix B for details). For all of the above reasons, in the following of this study, only the circular polarizations will be analyzed.

### B. Sensitivity to Topography and Soil Moisture

In order to analyze the effect of the large-scale roughness, i.e., the topography, on LR and RR signals and ratios, SAVERS simulations were carried out along a SP track passing over a mountainous area. The GNSS-R system configuration of TDS-1 acquisitions over the Tibesti volcanic region in Chad (top panel in Fig. 5) was used to set up SAVERS inputs (the same track was analyzed in [25] but considering single polarization data only).

In this analysis, the topography of the simulation area is taken into account in the computation of the reflected signal, by giving as input to the simulator the DEM of the area. The simulation resolution is 300 m. A dry and rough soil surface is assumed to be homogeneously present along the track (i.e., SR height standard deviation 3.5 cm and SM 5%). The IA increases from  $23^\circ$  to  $25.7^\circ$  when the latitude increases. As shown in Fig. 5, top panel, the DEM surface elevation (dashed orange line) around the SP is characterized by a significant variation, from 500 to 2500 m, as well as the slope is highly variable. Fig. 5 reports the simulated LR and RR reflectivity for each SP along the track. Left- and right-polarized reflectivity have a similar pattern along the track showing a decrease when the surface elevation increases. This is due to the large values and variability of the slopes over the mountainous areas, which causes a large variability of the local IA in the observed area and the loss of the specular condition for several illuminated surface elements.

Due to the similar sensitivity of the two polarizations to the topography, the RR/LR polarization ratio is slightly affected by this surface parameter, as shown by the almost flat pattern of the red markers in the top panel of Fig. 5.

The reflectivity ratio slightly increases along the track because of the IA increase from lower to higher latitudes.

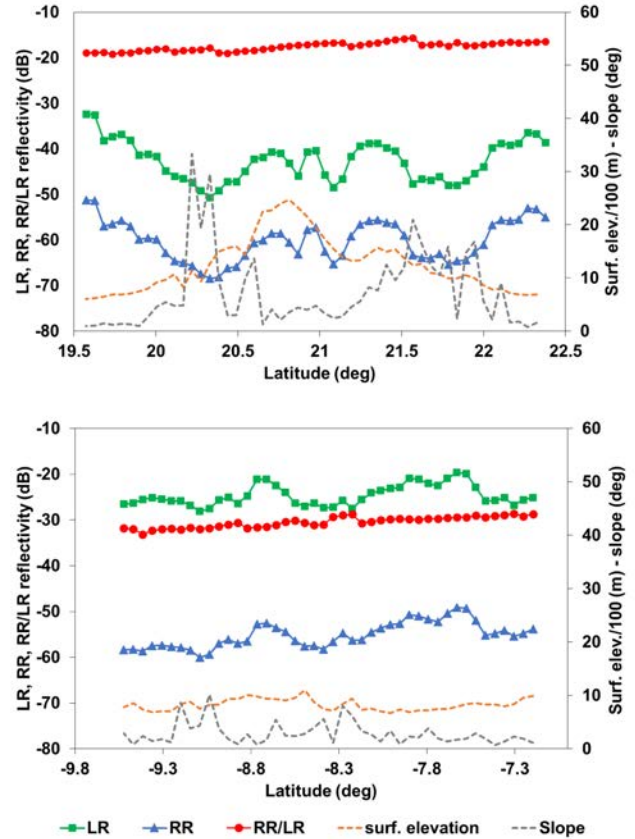


Fig. 5. LR, RR, and RR/LR bare soil simulations, surface elevation, and slope at SP along TDS-1 tracks. (Top) Track over a complex topography with approx.  $24^\circ$  IA. (Bottom) Track over a gentle topography with approx.  $10^\circ$  IA.

Indeed, as RR increases with the IA, the simulated difference between the LR and RR reflectivity decreases from 18.8 dB at  $23.1^\circ$  (latitude  $19.57^\circ$ ) to 16.4 dB at  $25.4^\circ$  (latitude  $22.37^\circ$ ).

The dependence of the polarization ratio on the IA is more evident in case of GNSS-R observations having an IA lower than  $15^\circ$ , due to the higher sensitivity of RR to the angle. This is the case of the simulations shown in the bottom panel of Fig. 5. In this plot, the simulation along a TDS-1 track passing over a gentle topography in Congo is reported, where the IA varies along the track from  $9.9^\circ$  at  $-9.52^\circ$  latitude to  $12^\circ$  at  $-7.19^\circ$  latitude (a bare surface was simulated with 2.0 cm SR and 15% SM along the track). The surface elevation and slope have a smaller variability range along this track than in Chad but the small variations of the local IA introduced by the topography lead to larger variations of RR and to a pattern of the polarization ratio less stable than for the Chad track.

The sensitivity of the ratio RR/LR to SM over a real topography was investigated by assuming a variation of SM along the track. In this test, the SP track of TDS-1 over an area with a gentle topography near the Tibesti region in Chad was considered. Along the track, the surface elevation ranges from 300 to 600 m and the IA ranges from  $21^\circ$  to  $23^\circ$ . In the top panel of Fig. 6, the simulated LR and RR reflectivity is reported as a function of the SP latitude for the case of a homogeneously constant SM of 5%.



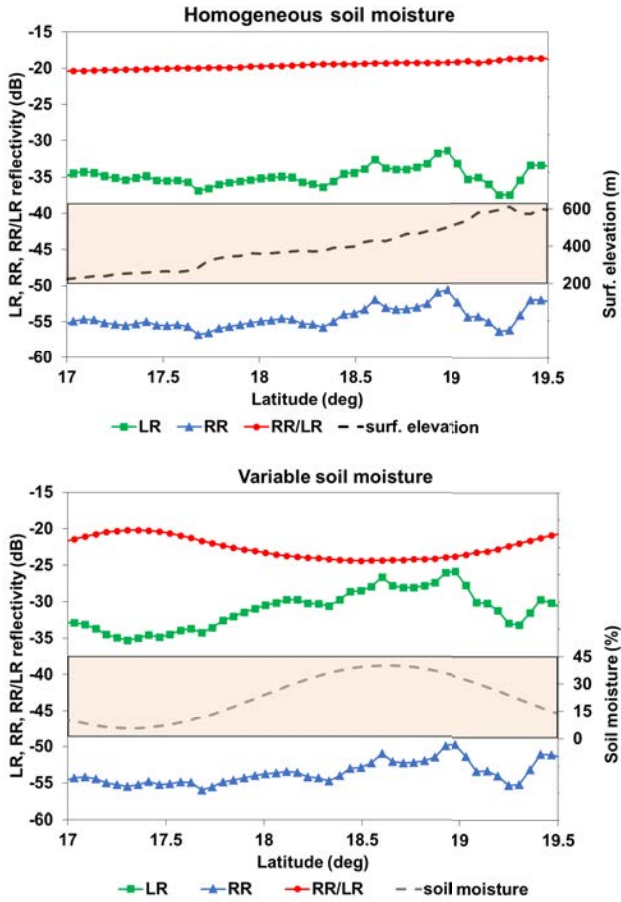


Fig. 6. LR, RR, and RR/LR bare soils simulations along a track passing over a gentle topography. (Top) Homogenous SM for all SPs of the track; the surface elevation is reported in the inset rectangle. (Bottom) Variable SM along the track; the SM is reported in the inset rectangle.

The variations of the reflectivity along the track, similar for the two polarizations, are mainly due to the topography. The SP elevation (taken from the DEM) is reported in the shaded box as a dashed black line. The ratio RR/LR (red markers of Fig. 6 top panel) has a flat pattern, as it is not significantly affected by the topography.

When a variation of SM is assumed along the track, as reported in the orange box of the bottom panel of Fig. 6 (gray dashed line), the pattern of LR reflectivity is clearly affected by a combination of topography and SM variations, and the ratio RR/LR clearly follows the SM variations.

Having substantially removed the topography effect, the sensitivity to SM is singled out by the RR/LR ratio. Therefore, this ratio can potentially perform better than a single polarization (LR only) for the SM retrieval in the presence of gentle and complex topography.

C. Sensitivity to Biomass Without Topography

The sensitivity of the LR and RR reflectivity to forest BIO was analyzed assuming a surface with a homogeneously constant elevation (i.e., without topography) covered by a boreal forest.

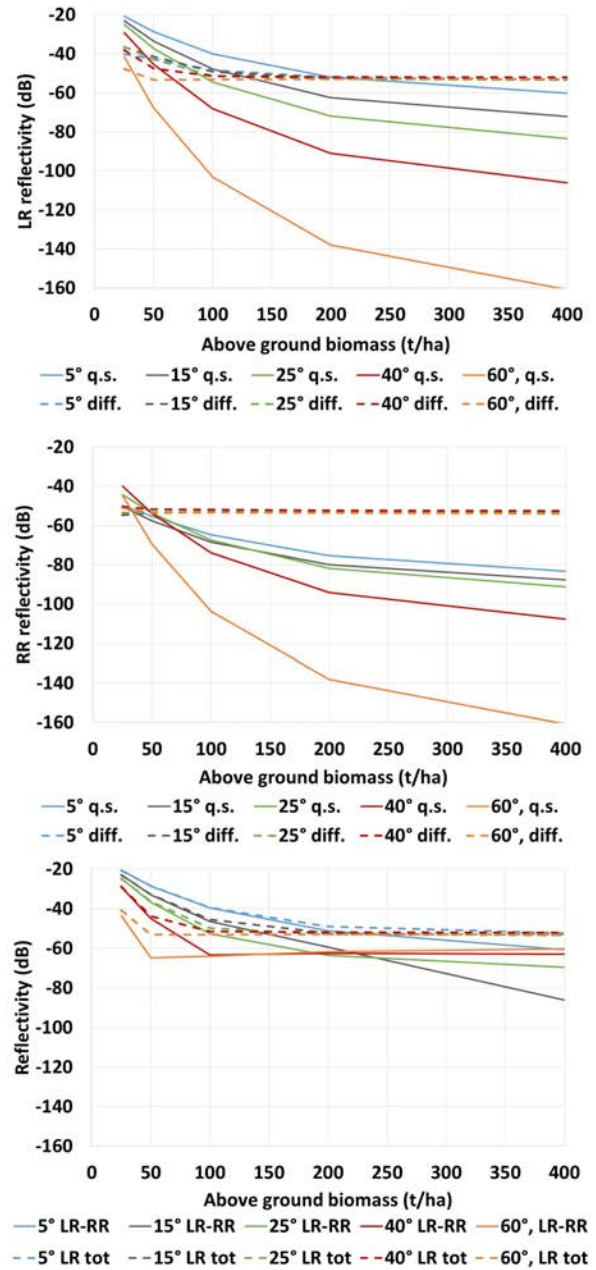


Fig. 7. (Top and middle) simulated quasi-specular (continuous line) and diffuse (dashed line) reflectivity versus BIO of a boreal forest for LR (top) and RR (middle) polarization. Different colors refer to different IAs. (Bottom) LR total reflectivity (dashed line) and LR-RR (continuous line) versus BIO.

The above ground BIO was increased from 25 t/ha to 50, 100, 200, and 400 t/ha (the other vegetation parameters were varied accordingly: diameter at breast height (dbh) from 7 to 21 cm, tree density from 700 to 950 trees per hectare, and leaf area index (LAI) between 0.5 and 8 m<sup>2</sup>/m<sup>2</sup>).

The IA ranged between 5° and 60°, with a step of 5°; the volumetric SM ranged between 5% and 40% with a step of 5%; and the SR was set to 0.5, 1.5, and 3.0 cm. Fig. 7 shows the LR-polarized (top panel) and RR-polarized (middle panel) reflectivity simulated by SAVERS over the forest.

TABLE IV

MEAN VARIATIONS OF LR, RR, RR/LR, LR-RR, AND  $NPD_{L,R}$  FOR THE VARIATION OF BIO FROM 25 t/ha TO 100 t/ha (BIO < 100) AND FROM 100 TO 400 t/ha (BIO > 100), OF SM FROM 5% TO 40%, OF SR FROM 0.5 TO 3.0 cm, AND OF IA FROM 5° TO 60°. CASE STUDY: SOFTWOOD FOREST

	LR	RR	RR/RR	LR-RR	$NPD_{L,R}$
$\Delta_{BIO < 100}$ (dB)	-19.4	-7.1	12.3	-25.1	-7.3
$\Delta_{BIO > 100}$ (dB)	-3.7	-0.5	3.2	-10.7	-7.8
$\Delta_{SM}$ (dB)	2.7	0.7	-2.2	4.4	1.9
$\Delta_{SR}$ (dB)	-5.7	-2.3	3.4	-8.1	-2.8
$\Delta_{IA}$ (dB)	-10.6	0.4	11.0	-16	-6.9

Both the quasi-specular component (the continuous lines in top and middle panels of Fig. 7) and the incoherent diffuse component (dashed lines) of the signal are reported in the plots. In order to simplify the plots, only the simulations obtained for a 25% SM, a 1.5 cm roughness, and 5°, 15°, 25°, 40°, and 60° IA are here shown.

The quasi-specular component of both LR and RR signal, which is due to the soil contribution attenuated by the vegetation, is strongly sensitive to the BIO increase, as it was also shown in [2]. However, it can reach extremely low reflectivity values at high IAs. The LR quasi-specular signal at 5° IA decreases by about 40 dB in the analyzed BIO range, and by about 119 dB at 60°. The decrease of the LR reflectivity is steeper for lower biomasses. A total decrease of about 34 dB of the RR quasi-specular reflectivity is observed when the BIO increases from 25 to 400 t/ha at 5° IA and by about 116 dB at 60°. Therefore, the quasi-specular RR signal is slightly less sensitive to BIO than the LR.

The incoherent diffuse component, due to vegetation volume scattering, is sensitive to BIO up to 100 t/ha for the case of LR polarized signal, and it is insensitive to BIO for the case of RR signal. Moreover, the diffuse component becomes dominant at high BIO values, since the soil quasi-specular reflection is very much attenuated by the above vegetation, thus causing the saturation of the total reflectivity.

As for the LR polarization, the total reflectivity reaches the saturation at about 200 t/ha at 5° IA and for a much lower BIO at 60° IA (Fig. 7 bottom panel, dashed line). The RR signal is already saturated at very low BIO values, i.e., at about 50 t/ha. Therefore, on average, the total LR polarized signal varies about 0.7 dB per 10 t/ha BIO variation (in the BIO range from 25 to 400 t/ha) and the total RR polarized signal varies about 0.2 dB per 10 t/ha BIO variation. For this reason, the variation of LR due to the BIO increase reported in Table IV is higher than the RR variation, for both low (<100 t/ha) and high (>100 t/ha) BIO ranges. From the same table, it is possible to conclude that both LR and RR are less sensitive to SM under the forest than over bare soils and depend on both SR and IA.

The incoherent diffuse component of the two polarizations reaches a similar value when saturated. For this reason, the computation of the difference LR-RR (the absolute difference is computed in linear units and then it is reported in dB in

the bottom panel of Fig. 7) results in deleting the diffuse component, which was the cause of the saturation, and in singling out the quasi-specular component. The difference LR-RR is compared to the total LR reflectivity (sum of the quasi-specular and diffuse component) in the bottom panel of Fig. 7. For IAs lower than 30°, LR-RR does not saturate even at high BIO values, but it remains sensitive to the BIO above the saturation threshold of the LR signal. Whereas, at IAs higher than 30°, LR-RR saturates as LR. The highest sensitivity is found at 15° IA: on average, the difference LR-RR varies about 1.8 dB per 10 t/ha BIO variation over the complete BIO range between 25 and 400 t/ha. The variation of the polarization difference due to BIO variations reported in Table IV confirms that the LR-RR is more sensitive to BIO for both low and high values of this parameter than LR. For completeness, the variations of the polarization ratio and of the  $NPD_{L,R}$  for the case of forest are reported in Table IV as well. However, the ratio is less suitable for the BIO monitoring because it does not remove the diffuse component and therefore the sensitivity of this observable to high biomasses is relatively low (see  $\Delta_{BIO > 100}$ ).  $NPD_{L,R}$  has a lower  $\Delta_{BIO}$  than the polarization difference. It is worth mentioning that the ratio and  $NPD_{L,R}$  are still, though slightly, sensitive to SR when the surface is covered by a forest, as it is shown by the  $\Delta_{SR}$  in Table IV.

#### D. Sensitivity to Forest Biomass With Topography

The effect of the topography on the sensitivity of the two polarizations to the BIO was investigated considering the DEM surface elevation and slope in the SAVERS simulations.

The GNSS-R system configuration of a TDS-1 acquisition was used to set up SAVERS inputs and the simulations were repeated for all SPs of a track passing over an area with a gentle topography in Congo (surface elevation, ranging between 800 and 1450 m, is reported in Fig. 8(a) with a dashed orange line).

The IA increases from 16.3° to 18.8° moving from -9.19° latitude to -12.43° latitude. A homogeneous SM equal to 20% and a value of SR height standard deviation equal to 1.5 cm were assumed in the simulation area for all SPs of the track.

First, the simulation was carried out for the case of a bare soil to single out the effect of the topography on the received signal for both polarizations [see Fig. 8(a)]. Then, the simulation was repeated assuming the presence of a boreal forest with a variable BIO along the track (red dashed line in the plots of Fig. 8). Three variability ranges of BIO were considered: lower than 150 t/ha (corresponding to the BIO values provided in [34] for that track) in Fig. 8(b), between 120 and 250 t/ha in Fig. 8(c), and between 220 and 350 t/ha in Fig. 8(d). The last two ranges were obtained increasing the values in [34] by 100 and 200 t/ha, respectively. The plots of Fig. 8 show the total LR (green), the total RR (blue), and the LR-RR (black) reflectivity along the track.

For the case of bare soils [Fig. 8(a)], the effect of the topography causes the variations of the reflectivity. LR and RR signals have similar sensitivity to the topography and differ by

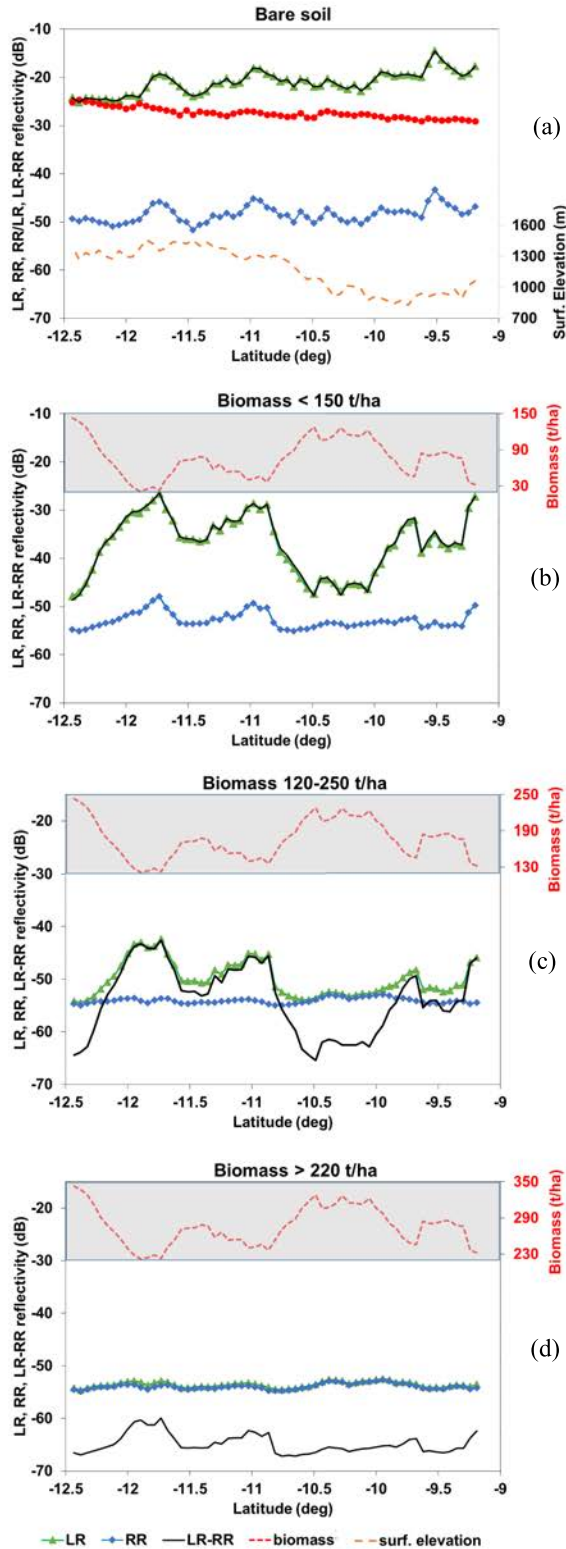


Fig. 8. LR, RR, and LR-RR simulated reflectivity along a track passing over a gentle topography for the case of (a) bare soil and (b) boreal forest with a variable BIO along the track in the following ranges: lower than 150 t/ha, (c) between 120 and 250 t/ha, and (d) between 220 and 350 t/ha.

about 24 dB. In the same plot, it is possible also to see that the RR/LR ratio is independent of the topography, whereas

TABLE V  
PEARSON COEFFICIENT OF LR, RR/LR, LR-RR,  
AND NPD WITH FOREST BIO

	LR	RR/LR	LR-RR	NPD
Biomass<150t/ha	-0.97	0.96	-0.98	-0.85
120<BIO<250t/ha	-0.91	0.94	-0.98	-0.95
Biomass>220t/ha	-0.07	0.80	-0.81	-0.86

the LR-RR difference remains sensitive to this surface feature (note that the LR and LR-RR curves are almost overlapped because of the low values of RR).

As already discussed in Section IV-C, the plots of Fig. 8 for the case of forest show that the vegetation attenuates the soil contribution: the higher is the BIO, the higher is the attenuation and the lower is the reflectivity.

When the forest BIO is lower than 150 t/ha [Fig. 8(b)], LR reflectivity is very sensitive to BIO variations, whereas the pattern of RR reflectivity is much flatter than that of LR. In Fig. 8(b), LR-RR reflectivity is approximately equal to the LR, as the latter is much higher than the RR reflectivity.

When the BIO ranges between 120 and 250 t/ha [Fig. 8(c)], LR signal reaches the saturation above the 200 t/ha and RR is saturated along the whole track. However, the LR-RR difference keeps the sensitivity to the BIO along the whole track, even above 200 t/ha.

For a BIO higher than 220 t/ha [Fig. 8(d)], both LR and RR signals are saturated, but LR-RR still shows a variation along the track related to the variations of BIO.

The Pearson coefficient was computed to compare the correlation of a single polarization with the BIO and the correlation of the polarization difference, the polarization ratio, and the NPD over a realistic topography (see Table V).

The polarization difference largely improves the correlation when the BIO reaches values higher than 220 t/ha (Pearson coefficient of  $-0.81$ ), with respect to the uncorrelated single polarization (Pearson coefficient of  $-0.07$ ) and has a higher correlation when the BIO ranges between 120 and 250 t/ha. On average, the polarization difference performs better than the ratio and NDP over the complete range of BIO.

However, it must be remarked that both LR and RR polarized signals reach very low reflectivity values that can hardly be detected over a forest with high BIO.

## V. CONCLUSION

SAVERS simulator was used in this study to investigate the potential of polarimetric GNSS-R observations over land. The reliability of SAVERS simulations of LR and RR circularly polarized signals was first qualitatively assessed against GLORI airborne GNSS-R data. Then, a sensitivity analysis of LR and RR polarized signal to SM, SR, and BIO was carried out both excluding and including the effect of the topography.

The simulations over bare soils showed a comparable sensitivity of LR and RR signals to SR and a higher sensitivity of LR to SM (1.8 dB for a 10% variation of SM). Therefore, the combination of RR and LR observations, i.e., the ratio RR/LR (computed in linear units) can compensate for the effect of

the small-scale SR and can single out the effect of the SM. The sensitivity of RR/LR ratio to SM is similar to that of LR and this sensitivity does not change with the IA. Moreover, the RR/LR ratio has the advantage to strongly attenuate the effect of the large-scale surface roughness, even for areas with a complex topography. However, this ratio remains sensitive to the IA variations, like the RR-polarized signal.

The suitability of the polarization difference and of the  $\text{NPD}_{L,R}$  for the SM retrieval over bare soils was also investigated. Having the same features of LR, the polarization difference does not add any advantage. The sensitivity of the  $\text{NPD}_{L,R}$  to SM strongly depends on the IA (i.e., no sensitivity at low IAs).

The sensitivity analysis was extended also to the linearly polarized signal HR and VR (circularly transmitted and linearly received). The SAVERS simulations for the linear polarization over a bare soil were indirectly validated with the results found in literature and obtained from SMAP-R data, showing the reliability of the simulations. It was found that the two linearly polarized reflectivity are very similar over a bare soil and are 3 dB lower than LR at low IAs. Both HR and VR are sensitive to the SM, increasing approximately 2 dB for every 10% increase of the SM and have a similar sensitivity to SR. Therefore, the linear polarization ratio and the  $\text{NPD}_{H,V}$  are not affected by the SR. However, the sensitivity of the linear polarization ratio VR/HR to SM depends on the IA (i.e., no sensitivity at low IAs).

An advantage of the circularly polarized receivers with respect to the linear ones has been remarked in Appendix B. It is well known that the ionosphere introduces a rotation of the polarization plane of the linear electromagnetic fields that induces a mismatch with the receiving linear antenna. For this reason, the Faraday rotation angle before and after reflection on the Earth surface must be properly corrected. Instead, the amplitude of the signal received by a circularly polarized antenna is affected by the ionospheric Faraday rotation only for the transmitter to Earth path. And the latter can be neglected when the axial ratio of the GNSS signal is low, as it is expected to be for the Galileo satellites.

In case of a boreal forest, LR was found to be sensitive to BIO: on average, 0.7 dB per 10 t/ha of BIO variations in the range between 25 and 400 t/ha. For a BIO above 200 t/ha, the volume scattering becomes dominant and the LR signal reaches the saturation. Due to the much lower RR reflectivity values, the RR signal is already saturated for a BIO of about 50 t/ha. The predominant sensitivity of LR to the attenuation of soil quasi-specular reflection and the comparable LR and RR volume scattering make the combination of the two polarizations quite effective in the BIO retrieval. Indeed, the difference between LR and RR (computed in linear units) removes the diffuse component and singles out the quasi-specular component. For this reason, LR-RR enhances the sensitivity to BIO (between 1.2 and 1.8 dB per 10 t/ha BIO variation, at 5° and 15° IA, respectively) and extends the sensitivity range to BIO values above the saturation threshold of a single polarization and of radar observations at the same frequency. However, the LR-RR difference is sensitive to the

large-scale surface roughness, in particular for low BIO, and this can introduce uncertainties in the BIO retrieval over gentle and complex topography.

Based on the discussion outlined above, the synergic use of two circular polarizations can potentially enhance the GNSS-R capability for SM and BIO monitoring, as long as the receiving sensor is able to measure very low levels of reflectivity with sufficiently high accuracy. This represents a major challenge with respect to the present spaceborne configurations because of the typical antenna pattern of a GNSS-R systems. As outlined in Section IV, most SPs with an IA larger than 50° are discarded because they have a low SNR, i.e., the reflected power falls beyond the -10 dB antenna beamwidth, or even at the first nulls of the antenna pattern. An increase of the antenna gain corresponds to reduce its beamwidth, thus reducing further the number of observable SPs.

To overcome this criticality, ad hoc strategies should be implemented by future missions, such as the possibility of steering high-gain beams at the SP optimizing the orbit height, and achieving relatively low values of the noise figure of the receiver.

## APPENDIX

### A. Covariance Matrix

The polarization dependence of the bistatic radar equation is ruled by the radar cross section in (1) that, in turn, depends on the electromagnetic approximation applied to evaluate the scattering function  $S_{pq}$  in (3). The matrix  $S$  of the target relates the incident field  $\mathbf{E}^i$  to the scattered field  $\mathbf{E}^s$  by means of

$$\mathbf{E}^s = \begin{pmatrix} E_p^s \\ E_q^s \end{pmatrix} = \frac{e^{-ikR}}{R} \begin{pmatrix} S_{pp} & S_{pq} \\ S_{qp} & S_{qq} \end{pmatrix} \begin{pmatrix} E_p^i \\ E_q^i \end{pmatrix} = \frac{e^{-ikR}}{R} \underline{\mathbf{S}} \mathbf{E}^i \quad (\text{A1})$$

where  $k = 2\pi/\lambda$  is the wavenumber in free space, and  $R$  is the distance between the scatterer and the receiving antenna. The scattering matrix elements depend on the incidence and scattering angles, and on the target parameters.  $p$  and  $q$  represent two orthogonal components of the complex scattered and incident fields, respectively. They can be horizontal H and vertical V components in a linear basis, or right R and left L in a circular basis.  $S_{pq}$  are complex quantities that describe amplitude, phase, and polarization of the scattered wave.

If the harmonic time variability in the complex domain is assumed to be  $e^{i\omega t}$ , the polarization unit vectors in (2) in a linear basis are:  $\mathbf{p}_R^r = (1/\sqrt{2})\begin{pmatrix} 1 \\ -1 \end{pmatrix}$  for the GNSS transmitted or received right polarization,  $\mathbf{p}_L^r = (1/\sqrt{2})\begin{pmatrix} 1 \\ 1 \end{pmatrix}$  for the received left polarization,  $\mathbf{p}_V^r = \begin{pmatrix} 0 \\ 1 \end{pmatrix}$  for the received vertical polarization, and  $\mathbf{p}_H^r = \begin{pmatrix} 1 \\ 0 \end{pmatrix}$  for the received horizontal polarization.

Applying (1), it is possible to get the radar cross sections, given an incident right-polarized field

$$\begin{aligned}\sigma_{RR} &= 4\pi \left| \frac{S_{VV} - S_{HH} - \iota(S_{VH} + S_{HV})}{2} \right|^2 = 4\pi |S_{RR}|^2 \\ \sigma_{LR} &= 4\pi \left| \frac{S_{VV} + S_{HH} - \iota(S_{VH} - S_{HV})}{2} \right|^2 = 4\pi |S_{LR}|^2 \\ \sigma_{VR} &= 4\pi \left| \frac{S_{VV} + S_{VH}}{\sqrt{2}} \right|^2 = 4\pi |S_{VR}|^2 \\ \sigma_{HR} &= 4\pi \left| \frac{S_{HH} + S_{HV}}{\sqrt{2}} \right|^2 = 4\pi |S_{HR}|^2.\end{aligned}\quad (\text{A2})$$

At low IAs  $S_{VV} = S_{HH} = S_0$ , and both  $S_{HV}$  and  $S_{VH}$  are negligible with respect to  $S_0$ . As a consequence

$$\sigma_{LR} = \sigma, \quad \sigma_{RR} = 0, \quad \sigma_{VR} = \sigma_{HR} = \sigma/2. \quad (\text{A3})$$

In this condition, the highest radar cross section is observed for LR polarization, while both HR and VR polarizations are expected to be 3 dB lower.

### B. Faraday Rotation

The nominal polarization of the GNSS transmitted signal is the right hand circular. However, the antenna imperfections introduce a left-hand-polarized component that increases far from the antenna boresight giving rise to an elliptical polarized signal. In general, an electromagnetic field can be represented as the superposition of circularly polarized components, so that an elliptical wave in the circular basis ( $\hat{L}$ ) is given by

$$\vec{E}^c = \begin{pmatrix} E_R \\ E_L \end{pmatrix} \quad (\text{B1})$$

with  $E_R \neq E_L$ , being in general complex numbers. In this basis, a linearly polarized wave has  $E_R = \pm E_L$ .

If  $\vec{E}^c$  impinges on a target, the scattered field is

$$\begin{pmatrix} E_R^{sC} \\ E_L^{sC} \end{pmatrix} = \begin{pmatrix} S_{RR}^C & S_{RL}^C \\ S_{LR}^C & S_{LL}^C \end{pmatrix} \begin{pmatrix} E_R \\ E_L \end{pmatrix} = \mathbf{S}^C \begin{pmatrix} E_R \\ E_L \end{pmatrix} \quad (\text{B2})$$

where  $S_{pq}^C$  are the scattering functions in the circular basis (being  $p$  and  $q$ , respectively, the polarization of the scattered and incident wave, that can be equal to R and/or L). The propagation factor ( $e^{-ikR}/R$ ), here and in the following, is understood.

The power carried by the right and left components of the scattered wave is proportional to

$$\begin{aligned}|E_R^{sC}|^2 &= |S_{RR}^C|^2 |E_R|^2 + |S_{RL}^C|^2 |E_L|^2 + 2\Re\{S_{RR}^C S_{RL}^{C*} E_R E_L^*\} \\ |E_L^{sC}|^2 &= |S_{LR}^C|^2 |E_R|^2 + |S_{LL}^C|^2 |E_L|^2 + 2\Re\{S_{LR}^C S_{LL}^{C*} E_R E_L^*\}\end{aligned}\quad (\text{B3})$$

where  $\Re$  is the real part operator.

After transmission through the ionosphere, an elliptical wave becomes

$$\begin{pmatrix} E_R^{\text{Far}} \\ E_L^{\text{Far}} \end{pmatrix} = \begin{pmatrix} e^{i\Omega_t} & 0 \\ 0 & e^{-i\Omega_t} \end{pmatrix} \begin{pmatrix} E_R \\ E_L \end{pmatrix} = \mathbf{F}^{Ct} \begin{pmatrix} E_R \\ E_L \end{pmatrix} \quad (\text{B4})$$

where  $\Omega_t$  is the Faraday rotation angle from the transmitter to the Earth. As observed in [34], [35], the ionosphere introduces

a phase shift between the left and right components of an elliptical wave that is twice the Faraday rotation angle  $\Omega_t$ .

If  $\Omega_r$  is the Faraday rotation angle through the ionosphere from the Earth to the receiver, the scattered field is

$$\begin{aligned}\begin{pmatrix} E_R^{\text{Far}} \\ E_L^{\text{Far}} \end{pmatrix} &= \mathbf{F}^{Cr} \mathbf{S}^C \mathbf{F}^{Ct} \begin{pmatrix} E_R \\ E_L \end{pmatrix} \\ &= \begin{pmatrix} e^{i\Omega_r} & 0 \\ 0 & e^{-i\Omega_r} \end{pmatrix} \begin{pmatrix} S_{RR}^C & S_{RL}^C \\ S_{LR}^C & S_{LL}^C \end{pmatrix} \begin{pmatrix} E_R^{\text{Far}} \\ E_L^{\text{Far}} \end{pmatrix} \\ &= \begin{pmatrix} e^{i\Omega_r} (S_{RR}^C e^{i\Omega_t} E_R + S_{RL}^C e^{-i\Omega_t} E_L) \\ e^{-i\Omega_r} (S_{LR}^C e^{i\Omega_t} E_R + S_{LL}^C e^{-i\Omega_t} E_L) \end{pmatrix}\end{aligned}\quad (\text{B5})$$

and the power

$$|E_R^{\text{Far}}|^2 = |S_{RR}^C|^2 |E_R|^2 + |S_{RL}^C|^2 |E_L|^2 + 2\Re\{S_{RR}^C S_{RL}^{C*} E_R E_L^* e^{2i\Omega_t}\} \quad (\text{B6})$$

$$|E_L^{\text{Far}}|^2 = |S_{LR}^C|^2 |E_R|^2 + |S_{LL}^C|^2 |E_L|^2 + 2\Re\{S_{LR}^C S_{LL}^{C*} E_R E_L^* e^{2i\Omega_t}\}. \quad (\text{B7})$$

Upon comparison with (B4), it is observed that the ionosphere affects the amplitude of the scattered field only through the  $\Omega_t$  Faraday rotation angle, which is introduced along the transmitter to Earth path. As long as the cross-polarized component of the transmitted GNSS right-hand signal is small, the ionospheric effect on the circular polarized scattered signal is negligible.

### REFERENCES

- [1] V. U. Zavorotny, S. Gleason, E. Cardellach, and A. Camps, "Tutorial on remote sensing using GNSS bistatic radar of opportunity," *IEEE Geosci. Remote Sens. Mag.*, vol. 2, no. 4, pp. 8–45, Dec. 2014.
- [2] P. Ferrazzoli, L. Guerriero, N. Pierdicca, and R. Rahmoune, "Forest biomass monitoring with GNSS-R: Theoretical simulations," *Adv. Space Res.*, vol. 47, no. 10, pp. 1823–1832, May 2011.
- [3] D. Masters, "Initial results of land-reflected GPS bistatic radar measurements in SMEX02," *Remote Sens. Environ.*, vol. 92, no. 4, pp. 507–520, Sep. 2004.
- [4] E. Cardellach, F. Fabra, O. Nogués-Correig, S. Oliveras, S. Ribó, and A. Rius, "GNSS-R ground-based and airborne campaigns for ocean, land, ice, and snow techniques: Application to the GOLD-RTR data sets," *Radio Sci.*, vol. 46, no. 6, pp. 1–16, Dec. 2011.
- [5] A. Egido et al., "Global navigation satellite systems reflectometry as a remote sensing tool for agriculture," *Remote Sens.*, vol. 4, no. 8, pp. 2356–2372, Aug. 2012.
- [6] A. Egido et al., "Airborne GNSS-R polarimetric measurements for soil moisture and above-ground biomass estimation," *IEEE J. Sel. Topics Appl. Earth Observ. Remote Sens.*, vol. 7, no. 5, pp. 1522–1532, May 2014.
- [7] M. Zribi et al., "Airborne GNSS-R polarimetric multiincidence data analysis for surface soil moisture estimation over an agricultural site," *IEEE J. Sel. Topics Appl. Earth Observ. Remote Sens.*, vol. 15, pp. 8432–8441, 2022.
- [8] H. Carreno-Luengo, A. Camps, J. Querol, and G. Forte, "First results of a GNSS-R experiment from a stratospheric balloon over boreal forests," *IEEE Trans. Geosci. Remote Sens.*, vol. 54, no. 5, pp. 2652–2663, May 2016.
- [9] M. Unwin, P. Jales, J. Tye, C. Gommenginger, G. Foti, and J. Rosello, "Spaceborne GNSS-reflectometry on TechDemoSat-1: Early mission operations and exploitation," *IEEE J. Sel. Topics Appl. Earth Observ. Remote Sens.*, vol. 9, no. 10, pp. 4525–4539, Oct. 2016.
- [10] C. S. Ruf et al., "A new paradigm in Earth environmental monitoring with the CYGNSS small satellite constellation," *Sci. Rep.*, vol. 8, no. 1, p. 8782, Jun. 2018.
- [11] C. Chew et al., "SMAP radar receiver measures land surface freeze/thaw state through capture of forward-scattered L-band signals," *Remote Sens. Environ.*, vol. 198, pp. 333–344, Sep. 2017.
- [12] N. Pierdicca et al., "The potential of spaceborne GNSS reflectometry for soil moisture, biomass, and freeze-thaw monitoring: Summary of a European space agency-funded study," *IEEE Geosci. Remote Sens. Mag.*, vol. 10, no. 2, pp. 8–38, Jun. 2022.

- [13] C. Chew and E. Small, "Description of the UCAR/CU soil moisture product," *Remote Sens.*, vol. 12, no. 10, p. 1558, May 2020.
- [14] E. Santi et al., "Remote sensing of forest biomass using GNSS reflectometry," *IEEE J. Sel. Topics Appl. Earth Observ. Remote Sens.*, vol. 13, pp. 2351–2368, 2020.
- [15] K. Rautiainen, D. Comite, J. Cohen, E. Cardellach, M. Unwin, and N. Pierdicca, "Freeze–thaw detection over high-latitude regions by means of GNSS-R data," *IEEE Trans. Geosci. Remote Sens.*, vol. 60, 2022, Art. no. 4302713.
- [16] M. Morris, C. Chew, J. T. Reager, R. Shah, and C. Zuffada, "A novel approach to monitoring wetland dynamics using CYGNSS: Everglades case study," *Remote Sens. Environ.*, vol. 233, Nov. 2019, Art. no. 111417.
- [17] M. J. Unwin et al., "An introduction to the HydroGNSS GNSS reflectometry remote sensing mission," *IEEE J. Sel. Topics Appl. Earth Observ. Remote Sens.*, vol. 14, pp. 6987–6999, 2021.
- [18] E. Motte et al., "GLORI: A GNSS-R dual polarization airborne instrument for land surface monitoring," *Sensors*, vol. 16, no. 5, p. 732, May 2016.
- [19] H. Carreno-Luengo, S. Lowe, C. Zuffada, S. Esterhuizen, and S. Oveisgharan, "Spaceborne GNSS-R from the SMAP mission: First assessment of polarimetric scatterometry over land and cryosphere," *Remote Sens.*, vol. 9, no. 4, p. 362, Apr. 2017.
- [20] J. F. Munoz-Martin, X. Bosch-Lluis, N. Rodriguez-Alvarez, and K. Oudrhiri, "Calibration strategy for compact polarimetric GNSS-R instruments," *IEEE Trans. Geosci. Remote Sens.*, vol. 61, 2023, Art. no. 5103513.
- [21] N. Rodriguez-Alvarez, S. Misra, E. Podest, M. Morris, and X. Bosch-Lluis, "The use of SMAP-reflectometry in science applications: Calibration and capabilities," *Remote Sens.*, vol. 11, no. 20, p. 2442, Oct. 2019.
- [22] N. Pierdicca, L. Guerriero, R. Giusto, M. Brogioni, and A. Egido, "SAVERS: A simulator of GNSS reflections from bare and vegetated soils," *IEEE Trans. Geosci. Remote Sens.*, vol. 52, no. 10, pp. 6542–6554, Oct. 2014.
- [23] L. Guerriero et al., "Modeling of the GNSS-R signal as a function of soil moisture and vegetation biomass," in *Proc. IEEE Int. Geosci. Remote Sens. Symp.*, Jul. 2013, pp. 4050–4053.
- [24] L. Guerriero et al., "Ground-based remote sensing of forests exploiting GNSS signals," *IEEE Trans. Geosci. Remote Sens.*, vol. 58, no. 10, pp. 6844–6860, Oct. 2020.
- [25] L. Dente, L. Guerriero, D. Comite, and N. Pierdicca, "Space-borne GNSS-R signal over a complex topography: Modeling and validation," *IEEE J. Sel. Topics Appl. Earth Observ. Remote Sens.*, vol. 13, pp. 1218–1233, 2020.
- [26] J. D. Campbell et al., "Intercomparison of electromagnetic scattering models for delay-Doppler maps along a CYGNSS land track with topography," *IEEE Trans. Geosci. Remote Sens.*, vol. 60, 2022, Art. no. 2007413.
- [27] M. Zribi et al., "Potential applications of GNSS-R observations over agricultural areas: Results from the GLORI airborne campaign," *Remote Sens.*, vol. 10, no. 8, p. 1245, Aug. 2018.
- [28] V. U. Zavorotny and A. G. Voronovich, "Scattering of GPS signals from the ocean with wind remote sensing application," *IEEE Trans. Geosci. Remote Sens.*, vol. 38, no. 2, pp. 951–964, Mar. 2000.
- [29] D. Comite, F. Ticconi, L. Dente, L. Guerriero, and N. Pierdicca, "Bistatic coherent scattering from rough soils with application to GNSS reflectometry," *IEEE Trans. Geosci. Remote Sens.*, vol. 58, no. 1, pp. 612–625, Jan. 2020.
- [30] T.-D. Wu and K.-S. Chen, "A reappraisal of the validity of the IEM model for backscattering from rough surfaces," *IEEE Trans. Geosci. Remote Sens.*, vol. 42, no. 4, pp. 743–753, Apr. 2004.
- [31] F. T. Ulaby and D. Long, *Microwave Radar and Radiometric Remote Sensing*. Ann Arbor, MI, USA: Univ. Michigan Press, 2014.
- [32] R. K. Raney, "Hybrid dual-polarization synthetic aperture radar," *Remote Sens.*, vol. 11, no. 13, p. 1521, Jun. 2019.
- [33] N. Rodriguez-Alvarez, S. Misra, and M. Morris, "The polarimetric sensitivity of SMAP-reflectometry signals to crop growth in the U.S. corn belt," *Remote Sens.*, vol. 12, no. 6, p. 1007, Mar. 2020.
- [34] V. Avitabile, M. Herold, Heuvelink, S. L. Lewis, O. L. Phillips, and G. P. Asner, "An integrated pan-tropical biomass maps using multiple reference datasets," *Glob. Chang. Biol.*, vol. 22, no. 4, pp. 1406–1420, 2016.
- [35] S. Tomás, R. Padullés, and E. Cardellach, "Separability of systematic effects in polarimetric GNSS radio occultations for precipitation sensing," *IEEE Trans. Geosci. Remote Sens.*, vol. 56, no. 8, pp. 4633–4649, 2018.



**Laura Dente** received the Laurea degree in physics from the University of Bari, Bari, Italy, in 2000, and the Ph.D. degree from the University of Twente, Enschede, The Netherlands, in 2016.

In 2002, she was a Young Graduate Trainee at European Space Research and Technology Centre (ESTEC), Noordwijk, The Netherlands. From 2003 to 2006, she was a Research Fellow at the National Research Council (CNR), Institute of Intelligent Systems for Automation (ISSIA), Bari, on soil moisture and biomass retrieval from synthetic aperture radar (SAR) data. From 2007 to 2012, she was a Trainee Research Assistant at the International Institute for Geo-Information Science and Earth Observation (ITC) faculty of the University of Twente, Enschede, focusing on passive and active microwave remote sensing for soil moisture monitoring. From 2016 to 2023, she was a Research Fellow at the University of Rome Tor Vergata, Rome, Italy, where her main interests were GNSS-R and its application over land.



**Leila Guerriero** (Member, IEEE) received the Laurea degree in physics from the Sapienza University of Rome, Rome, Italy, in 1986, and the Ph.D. degree in electromagnetism from the Tor Vergata University of Rome, Rome, Italy, in 1991.

Since 1994, she has been a Permanent Researcher with the Tor Vergata University of Rome, where she is currently an Associate Professor holding courses on Earth Satellite Observation and on Geoinformation. She participated in several international projects such as the ESA projects Soil Moisture and Ocean Salinity Satellite; Development of SAR Inversion Algorithms for Land Applications; Use of Bistatic Microwave Measurements for Earth Observation; and SAOCOM-CS Bistatic Imaging, Radiometry and Interferometry Over Land. Lately, she has been involved in the modeling of Global Navigation Satellite System Reflectometry (GNSS-R) signals for ESA projects and in European FP7 and H2020 Programs. The most recent is the ESA Scout Mission HydroGNSS. Her research interests include modeling microwave scattering and emissivity from agricultural and forested areas.

Dr. Guerriero is a member of the Permanent Steering Scientific Committee of MicroRad. She is the Vice-President of the GRSS North-Central Italy Chapter.



**Emanuele Santi** (Senior Member, IEEE) received the M.S. degree in electronic engineering from the University of Florence, Florence, Italy, in 1997, and the Ph.D. degree in Earth's remote-sensing techniques from the University of Basilicata, Potenza, Italy, in 2005.

Since 1998, he has been with the Microwave Remote Sensing Group, Institute of Applied Physics, National Research Council, Florence. He was and is currently involved in many national and international projects funded by Italian Space Agency (ASI), European Community (EC), European Space Agency (ESA), and Japanese Aerospace Exploration Agency (JAXA), acting as the Team Leader, the WP Leader, and the Co-Investigator. He has authored or coauthored 191 articles, published on ISI journals and books and conference proceedings (source Scopus—H-index 27). His research interests include the development and validation of models and inversion algorithms based on machine learning for estimating the geophysical parameters of soil, sea, snow, and vegetation from microwave emission and scattering.

Dr. Santi is member of the "Centro di Telerilevamento a Microonde" (Microwave Remote Sensing Center), the Chair of the IEEE GRS Chapter CNI-29, and the Conference Chair of the SPIE Europe Remote Sensing conference RS-106. In 2020, he served as the Chair of the 16th Symposium on Microwave Radiometry MicroRad. In 2018, he received the IEEE GRSS J-STARS Prize Paper Award for the best paper published on IEEE JOURNAL OF SELECTED TOPICS IN APPLIED EARTH OBSERVATIONS AND REMOTE SENSING in 2017.



**Mehrez Zribi** (Senior Member, IEEE) received the B.E. degree in signal processing from the Ecole Nationale Supérieure d'Ingénieurs en Constructions Aéronautiques, Toulouse, France, in 1995, and the Ph.D. degree from the Université Paul Sabatier, Toulouse, in 1998.

In 1995, he joined the Centre d'Etude des Environnements Terrestre et Planétaires Laboratory, Institut Pierre Simon Laplace, Vélizy, France. Since October 2008, he has been with the Centre d'Etudes Spatiales de la Biosphère (CESBIO), Toulouse. He is a Research Director with the Center National de Recherche Scientifique (CNRS), Paris, France. He is currently the Director of Midi-Pyrénées Observatory. He has published more than 160 articles in refereed journals. His research interests include microwave remote sensing applied to hydrology, microwave modeling for land surface parameters estimations, and finally airborne microwave instrumentation.



**Davide Comite** (Senior Member, IEEE) received the master's degree (cum laude) in telecommunications engineering and the Ph.D. degree in electromagnetics and mathematical models for engineering from the Sapienza University of Rome, Rome, Italy, in 2011 and 2015, respectively.

He was a Visiting Ph.D. Student at the Institute of Electronics and Telecommunications of Rennes, University of Rennes 1, Rennes, France, in 2014, and a Post-Doctoral Researcher at the Center of Advanced Communications, Villanova University, Villanova, PA, USA, in 2015. He is currently a tenure track an Assistant Professor with the Sapienza University of Rome. His scientific interests currently involve Earth observation, remote sensing, the study of the scattering from natural surfaces, the GNSS reflectometry over land, as well as radar altimetry for biomass estimation. He is also interested in the study and design of microwaves and millimeter-waves antennas, antenna arrays, leaky waves, and leaky-wave antennas, as well as in the generation of nondiffracting waves and pulses.

Dr. Comite is an URSI Senior Member. From 2019 to 2022, the IEEE Antennas and Propagation Society recognized him as an Outstanding reviewer for IEEE TRANSACTION ON ANTENNAS AND PROPAGATION. In 2020, he was awarded as the best reviewer for the IEEE JOURNAL OF SELECTED TOPICS IN APPLIED EARTH OBSERVATION AND REMOTE SENSING. He currently serves as a reviewer for several international journals. He is an Associate Editor of the IEEE JOURNAL OF SELECTED TOPICS IN APPLIED EARTH OBSERVATION AND REMOTE SENSING, EurAAP Journal *Reviews of Electromagnetics*, the IET *Journal of Engineering*, the IET *Microwaves, Antennas, and Propagation* by the Institution of Engineering and Technology, and IEEE ACCESS. He has been leading the GNSS-R modeling Working Group of the GRSS MIRS Technical Committee since January 2021. From 2020 to 2022, he was one of the Officers of the Young Professional Affinity Group of the IEEE Italian Chapter. Since 2022, he is the Chair of the Early Career in Antenna and Propagation (ECAP) Working Group of EuRAAP.



**Nazzareno Pierdicca** (Senior Member, IEEE) received the Laurea degree (cum laude) in electronic engineering from Sapienza University of Rome, Rome, Italy, in 1981.

From 1978 to 1982, he was with Italian Agency for Alternative Energy (ENEA). From 1982 to 1990, he was with Telespazio, Rome, Italy, in the Remote Sensing Division. In November 1990, he joined the Department of Information Engineering, Electronics and Telecommunications, Sapienza University of Rome. He is currently a Full Professor and teaches remote sensing, antenna, and electromagnetic fields at the Faculty of Engineering, Sapienza University of Rome. His research interests include electromagnetic scattering and emission models for sea and bare soil surfaces and their inversion, microwave radiometry of the atmosphere, radar land applications, and bistatic radars.

Prof. Pierdicca is the past Chair of the GRSS Central Italy Chapter and the Chair of the GRSS Modeling in Remote Sensing Technical Committee.